Electronic Supplementary Information

Nonporous, conducting bimetallic coordination polymers with advantageous electronic structure for boosted Faradaic capacitance

*Yigang Jin, Sha Wu, Yong Sun, Zixin Chang, Ze Li, Yimeng Sun, and Wei Xu**

Beijing National Laboratory for Molecular Sciences, Key Laboratory of Organic Solids,

Institute of Chemistry, Chinese Academy of Sciences, Beijing 100190, China.

University of Chinese Academy of Sciences, Beijing 100049, China.

E-mail: wxu@iccas.ac.cn

Synthesis and characterizations

Synthesis of Ag_5BHT

Under argon atmosphere, 40 mL degassed isopropyl alcohol was added to the mixture of BHT (60 mg, 0.22 mmol) powder and Ag_2O (124 mg, 0.53 mmol) in 100 mL flask. The mixture was sonicated at 0 °C for 6 min, and then heated to 60 °C and stirred for 24 hours to form a dark green powder. After natural cooling to room temperature, the product was filtered, washed with water, CH_3OH, acetone and diethyl ether in sequence, and then dried at 80 °C under vacuum for 24 h. Yield: 166 mg (94%). Elem. Anal. Calcd. for $Ag_5C_6S_6$: C, 8.97; S, 23.93; Ag, 67.10. Found: C, 9.14; S, 23.91; Ag, 66.95.

Synthesis of $CuAg_4BHT$

Under argon atmosphere, $Cu(NO_3)_2•3H_2O$ (169 mg, 0.7 mmol) was dissolved in 120 mL degassed ethanol, and then Ag_5BHT (50 mg, 0.062 mmol) was added. The mixture was sonicated for 10 min, and subsequently heated to 80 °C with constant stirring for 72 h to form a gray-black powder, followed by natural cooling to room temperature. The obtained power was filtered, washed with water, ethanol, acetone, and diethyl ether in sequence, and then dried at 80 °C under vacuum for 24 h. Yield: 42 mg (89%). Elem. Anal. Calcd. For $CuAg_4C_6S_6$: C, 9.49; S, 25.33; Cu, 8.37, Ag, 56.81. Found: C, 9.72; S, 24.41; Cu, 9.01, Ag, 56.86.

Synthesis of Polyacrylamide (PAM) Hydrogel

0.32 g ammonium persulfate was dissolved in 10mL deionized water as solution (1). Then, 0.12 g N, N-bis-methacrylamide and 0.2 mL tetraformaldehyde ethylenediamine were dissolved in 10 mL deionized water as solution (2). 1g of acrylamide was dissolved in 5 mL of water, and added 0.05 mL of each of the (1), (2) solutions to the acrylamide solution and stirred for 3 min, then added the mixed solution to the mold and heated it at 60 °C for 30 min. Before assembling the two-electrode device, the dried gel was soaked in 1 M KCl aqueous solution for 12h.

Component characterizations

The content of carbon and sulfur were analyzed using Flash EA 1112 (Thermo Fisher Scientific). The metal content was analyzed by inductively coupled plasma-optical emission spectroscopy (ICP-OES, iCAP 6300 Radial, Thermo Scientific). For ICP-OES measurements, the samples were

prepared by dissolving them into fuming nitric acid. Then the resulting solution was diluted to a known volume with Milli-Q water. The metal to sulfur ratios were confirmed by EPMA (JEOL, JXA-8100). XPS was performed using AXIS Ultra-DLD ultrahigh vacuum photoemission spectroscopy system (Kratos Co.). All XPS spectra were calibrated by saturated carbon (C-C) C 1s peak at 284.8 eV. PXRD patterns were obtained at a PANalytical Empyrean II X-Ray diffractometer using Cu Kα radiation (λ = 1.5406 Å) at 40 kV and 40 mA. Before PXRD measurements, the samples have been well grounded. The specific surface areas of the samples were tested by Automatic specific surface and porosity analyzer BET (ASAP 2020HD88).

SEM and TEM characterizations

SEM images were captured using a Toshiba SU8000-SEM with an acceleration voltage of 10 kV. For the pretreatment, the samples were dispersed in ethanol and transferred to conductive silicon substrates, then covered with a layer of platinum a few nanometers thick. TEM and EDS images were acquired using a JEOL 2100F-TEM with an acceleration voltage of 120 kV. About 1 mg of the sample was dispersed in 4 mL of absolute acetone, and after ultrasonic dispersion for 30 min, 6 μL of the suspension was dropped on a copper grid coated with a carbon film to perform TEM characterizations.

Electrical property measurement

The electrical conductivities were measured on the pelletized samples via a four-probe method by using a KEITHLEY 2002 Multimeter (Keithley Instrument Inc.).

Electrochemical measurement

Cyclic voltammetry (CV), galvanostatic charge/discharge (GCD) measurements, and electrochemical impedance spectroscopy (EIS) were employed with a CHI 660E electrochemical workstation. EIS was recorded with open circuit voltage at AC amplitude of 5 mV in frequency range of 100 kHz to 0.01 Hz.

For a three-electrode system, the working electrodes were fabricated as followings: firstly, a mixture of active material (Ag_5BHT, $CuAg_4BHT$), polytetrafluoroethylene concentration (PTFE) and superconducting carbon black (American CABOT superconducting carbon black, BP 2000) with a weight ratio of 8: 1: 1 was thoroughly mixed and grounded in NMP to prepare a uniform slurry. Then, the slurry was uniformly coated on the conductive carbon paper (1 cm×1 cm). Similarly, the

AC slurry was prepared by mixing and grinding the mixture of commercial AC powder (Japan, Kuraray), PTFE and superconducting carbon black with a weight ratio of 8: 1: 1 in NMP. Then the slurry was uniformly coated on the conductive carbon paper to obtain AC electrodes. The prepared samples were dried in a dynamic vacuum oven at 80 °C for 12 hours to remove the solvent. The mass of loading active material on the sample is ~1 mg. Platinum plate and a saturated calomel electrode (SCE) electrode were used as the counter electrode and reference electrode, respectively. The gravimetric capacitance (C_m, F g^{-1}) and areal capacitance (C_s, F cm^{-1}) based on the CV curves were calculated using the following equation (1) and (2), respectively, where *m* is the mass of active material (g), *s* is the working area of electrode (cm^2), *v* is the scan rate (V s^{-1}), V_f and V_i are the integration potential limits of CV curves, *I(V)* is the voltammetric current (in amperes).

$$C_m = \frac{1}{2\times m\times v\times (V_f - V_i)} \int_{V_i}^{V_f} I(V)\, dV \qquad (1)$$

$$C_s = \frac{C_m \times m}{s} \qquad (2)$$

The gravimetric capacitance (C_m, F g^{-1}) based on the GCD curves were calculated using the following equation (3), where *I*/*m* is the current density (A g^{-1}), *t* is the discharge time (s), and *v* is the voltage range (V). When using formula (1) and formula (3) to calculate the gravimetric capacitance of the device, the mass of the active material is the sum of the mass of the active material on the two electrodes.

$$C_m = \frac{I}{m} \times \frac{t}{v} \qquad (3)$$

The $CuAg_4BHT$//AC device is constructed by using $CuAg_4BHT$ as the positive electrode material, AC as the negative electrode material, and PAM gel soaked in 1 M KCl aqueous solution as the separator and electrolyte. Meanwhile, in order to optimize the electrochemical performance of the prepared device, the charge storage in positive and negative electrodes were balanced according to the equation (3). C_m represents the gravimetric capacitance of the electrode, ΔV represents the potential window of the electrode, and *m* is the mass of active material.

$$\frac{m^+}{m^-} = \frac{C_m^- \Delta V^-}{C_m^+ \Delta V^+} \qquad (4)$$

The energy densities (*E*, Wh kg^{-1}) and power densities (*P*, W kg^{-1}) were calculated from equations (4) and (5), where $\triangle V$ is the discharge voltage range (*V*) and $\triangle t$ is discharge time (s).

$$E = \frac{C_m \Delta V^2}{2\times 3.6} \qquad (5)$$

$$P = \frac{E}{\Delta t} \times 3600 \qquad (6)$$

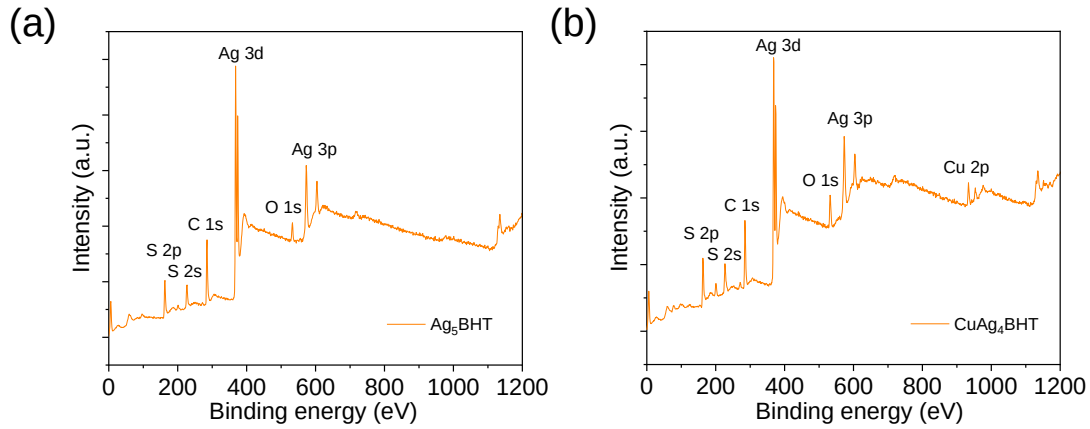

Figure S1. The XPS spectrum of Ag_5BHT and $CuAg_4BHT$.

(a)

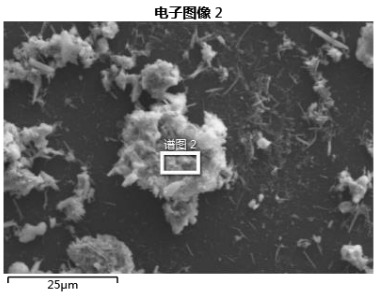

(b)

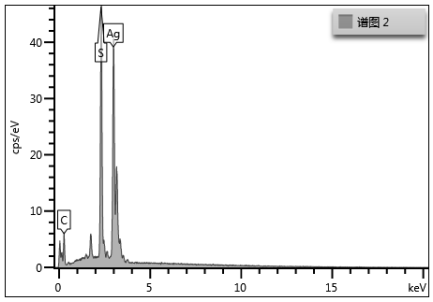

Element	At. NO.	Wt%	Wt% Sigma	Atom%
S	16	20.10	0.23	21.75
Ag	47	59.44	0.52	19.12
		Ag/S atomic ratio = 1: 1.14		

(c)

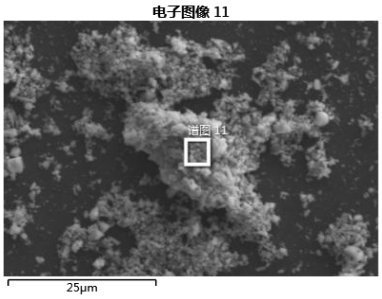

(d)

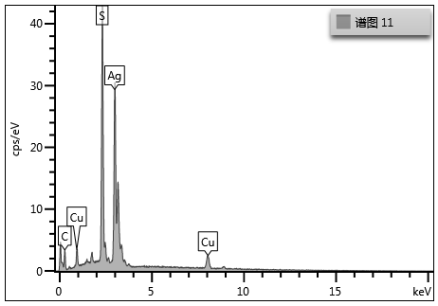

Element	At. NO.	Wt%	Wt% Sigma	Atom%
S	16	22.06	0.28	25.71
Cu	29	7.98	0.38	4.69
Ag	47	53.56	0.55	18.56
		Cu/Ag/S atomic ratio = 1: 3.96: 5.48		

Figure S2. The Electron Probe Micro-analyzer (EPMA) characterization performed on powder samples of Ag_5BHT (a,b) and $CuAg_4BHT$ (c,d). The corresponding element contents are listed in the tables below.

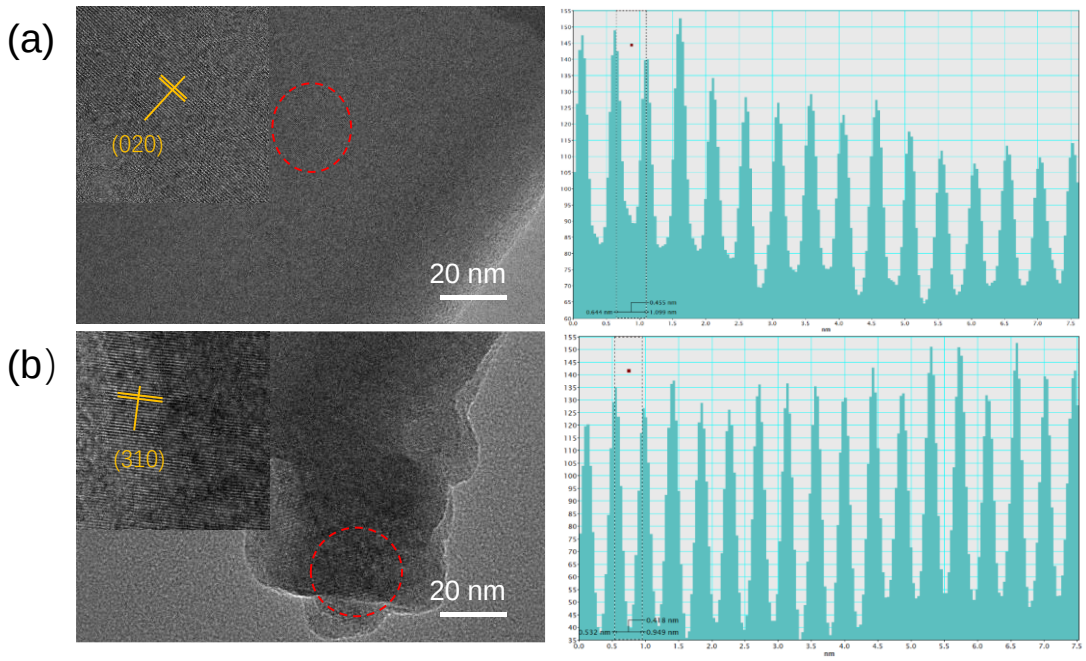

Figure S3. The high-resolution TEM (HR-TEM) pictures of Ag_5BHT (a) and $CuAg_4BHT$ (b).

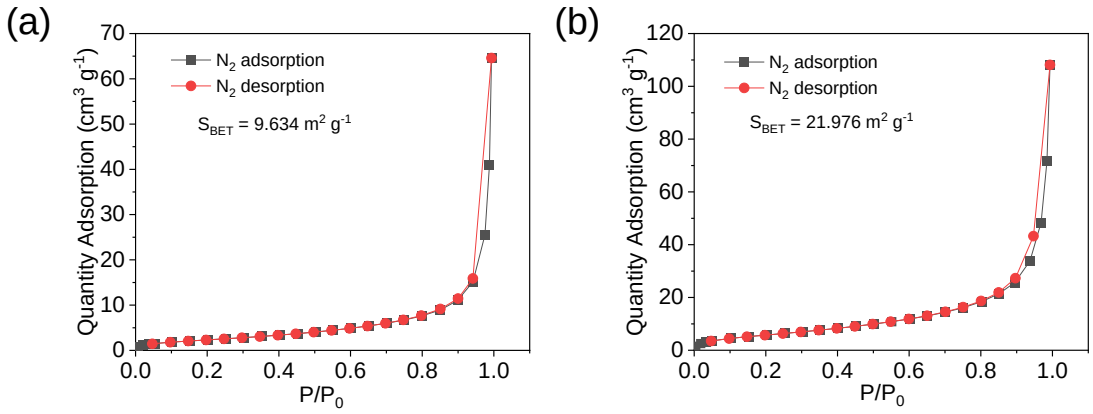

Figure S4. The gas sorption isotherm of Ag_5BHT (a) and $CuAg_4BHT$ (b) obtained using N_2 as the probe gas.

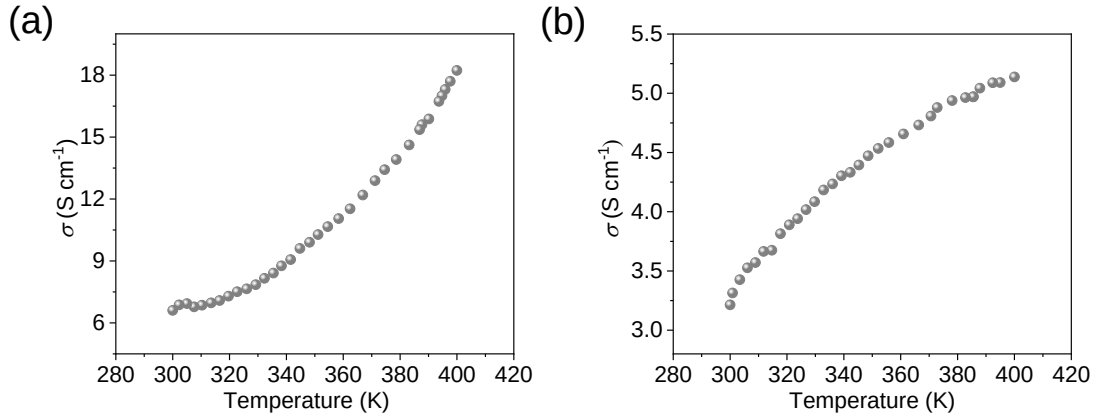

Figure S5. Electrical conductivities of the pellet samples of Ag_5BHT (a) and $CuAg_4BHT$ (b) as a function of temperature ranging from 300 K to 400 K.

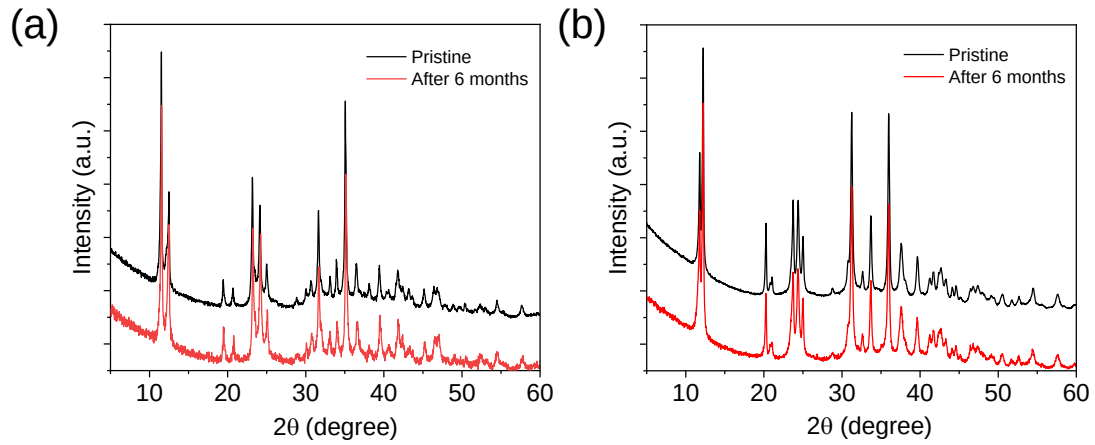

Figure S6. PXRD patterns of Ag_5BHT (a) and $CuAg_4BHT$ (b) samples before and after six months of air exposure.

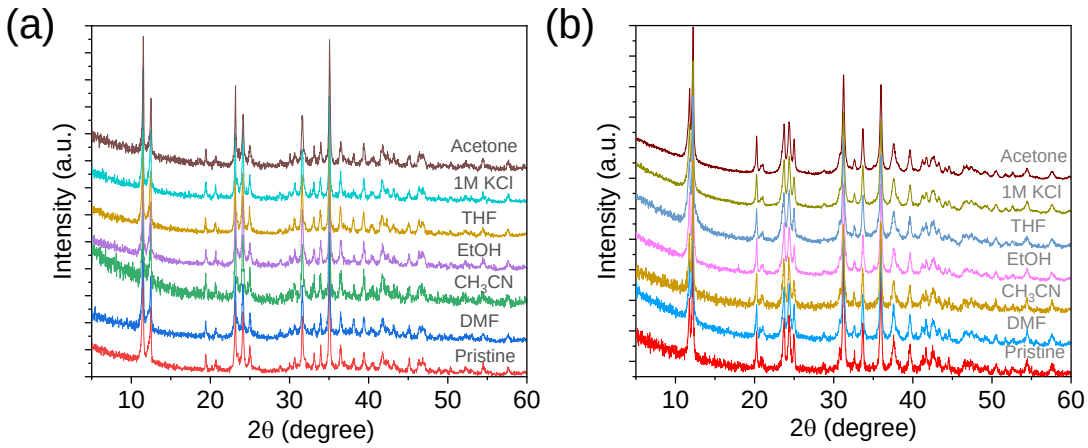

Figure S7. PXRD patterns of Ag_5BHT (a) and $CuAg_4BHT$ (b) after immersing in common solvents for three days.

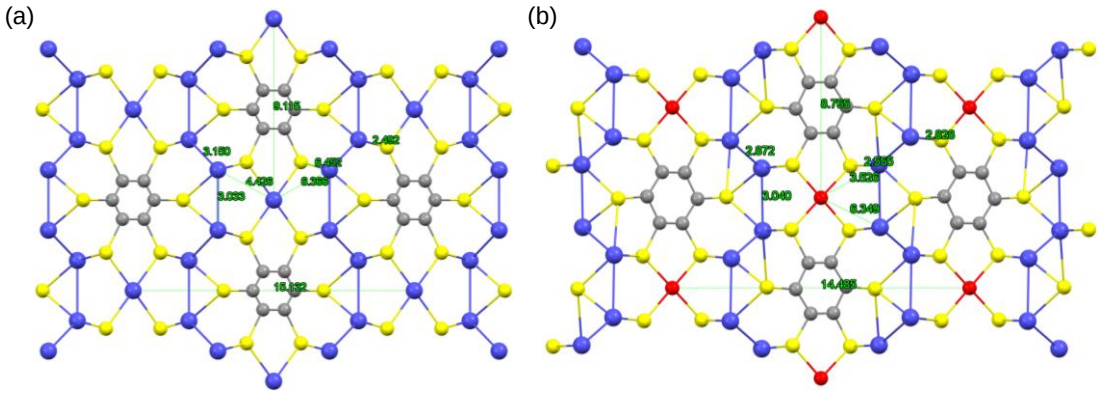

Figure S8. Illustration of the distances (Å) between different atoms in Ag_5BHT (a) and $CuAg_4BHT$ (b).

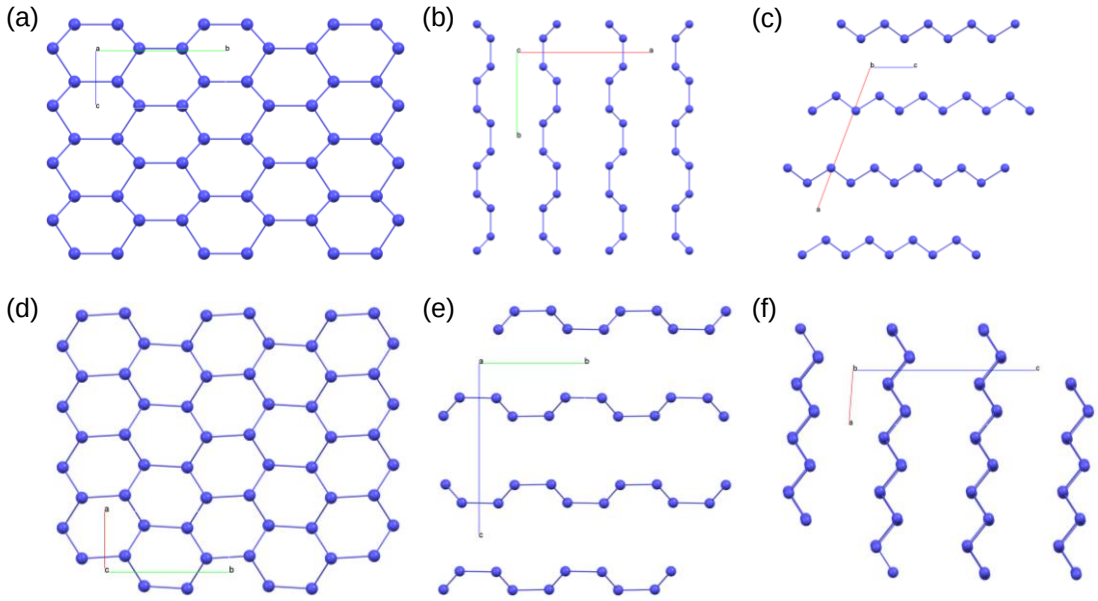

Figure S9. The graphene-like hexagonal motif of Ag atoms in Ag_5BHT (a-c) and $CuAg_4BHT$ (d-f) viewed along the different crystalline axis directions.

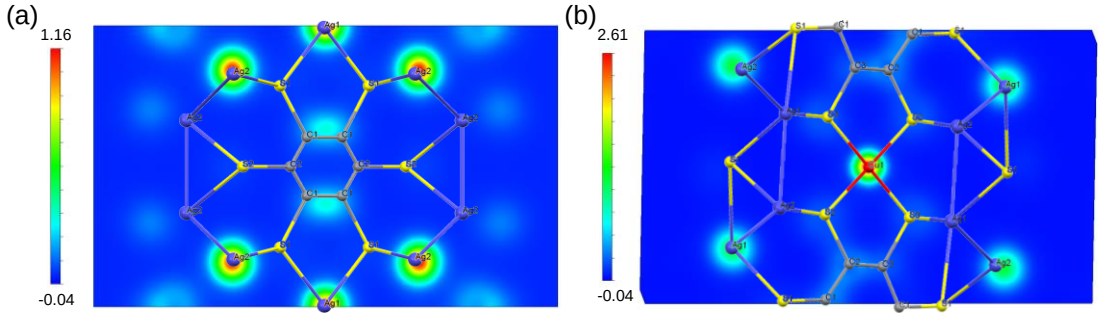

Figure S10. The charge density distributions of Ag_5BHT (a) and $CuAg_4BHT$ (b).

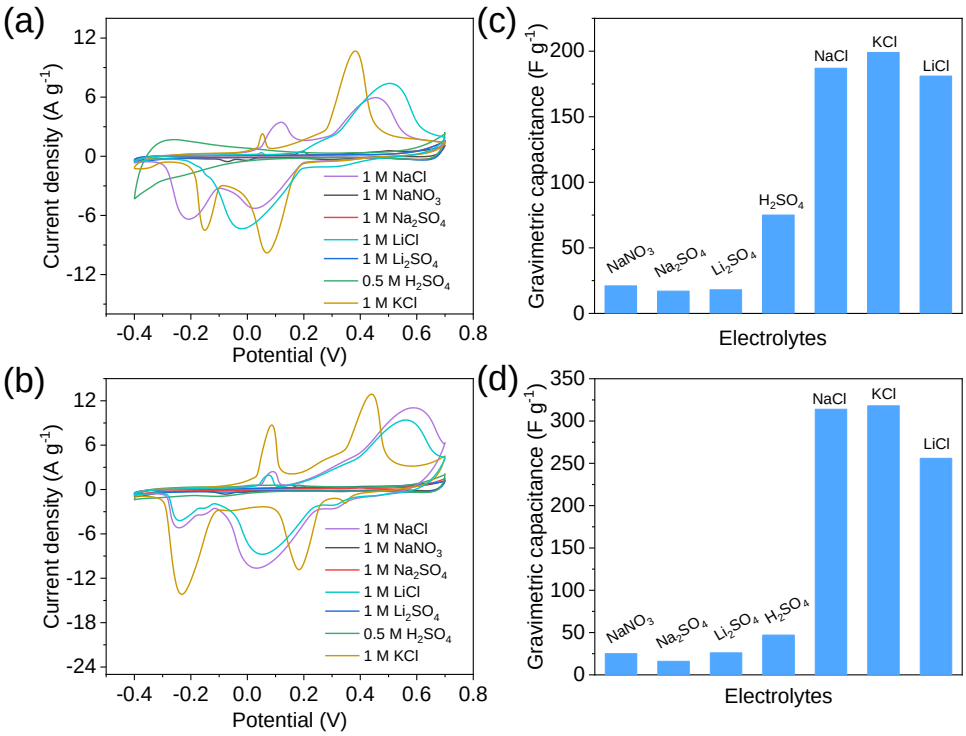

Figure S11. CV curves of Ag_5BHT (a) and $CuAg_4BHT$ (b) at 10 mV s^{-1} in different electrolytes. The gravimetric capacitances of Ag_5BHT (c) and $CuAg_4BHT$ (d) calculated from CV curves in different electrolytes.

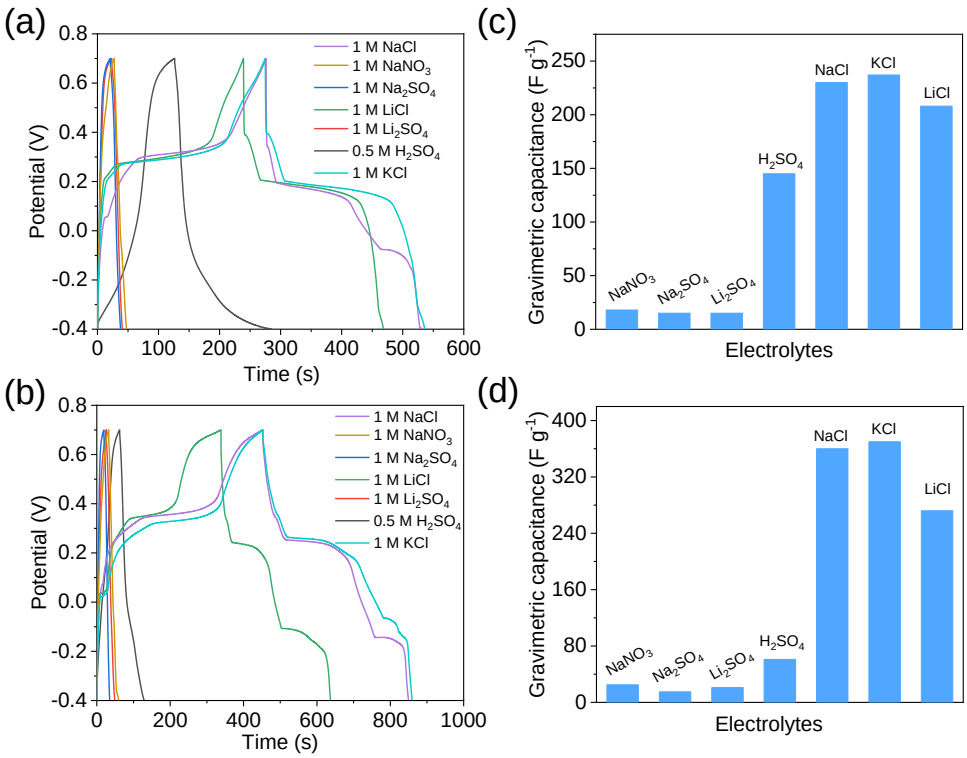

Figure S12. GCD curves of Ag_5BHT (a) and $CuAg_4BHT$ (b) at 1 A g^{-1} in different electrolytes. The gravimetric capacitances of Ag_5BHT (c) and $CuAg_4BHT$ (d) calculated from GCD curves in different electrolytes.

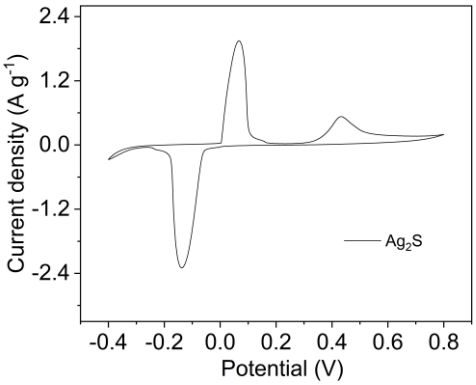

Figure S13. Cyclic voltammograms of Ag_2S on carbon paper in 1M KCl solution.

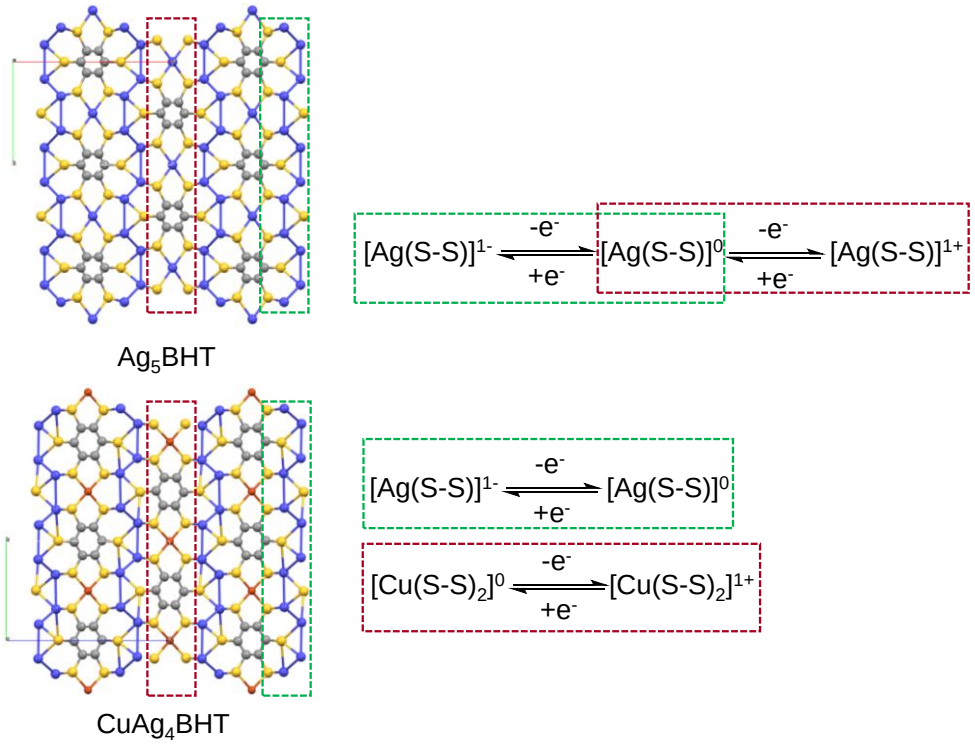

Figure S14. The possible redox mechanism of metal bis(dithiolene) coordination units during charge/discharge process.

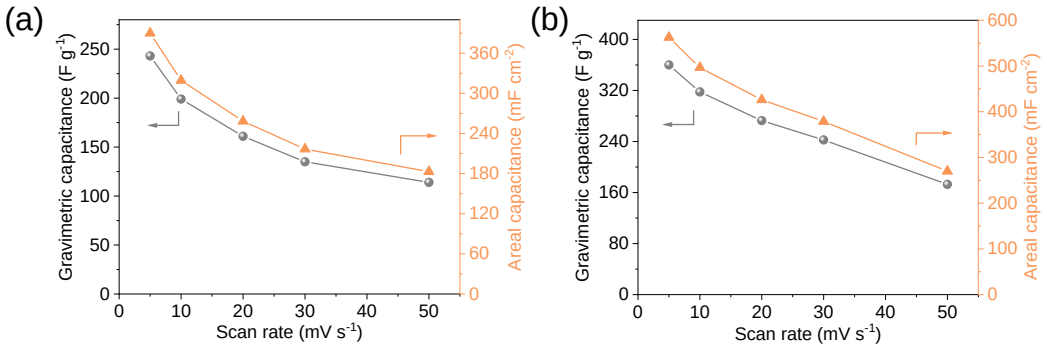

Figure S15. The comparison of gravimetric and areal capacitances of Ag_5BHT (a) and $CuAg_4BHT$ (b) at different scan rates.

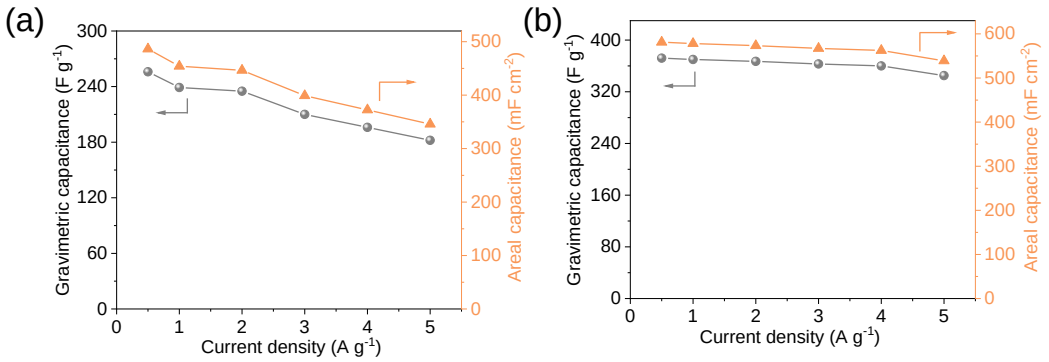

Figure S16. The comparison of gravimetric and areal capacitances of Ag_5BHT (a) and $CuAg_4BHT$ (b) at different current densities.

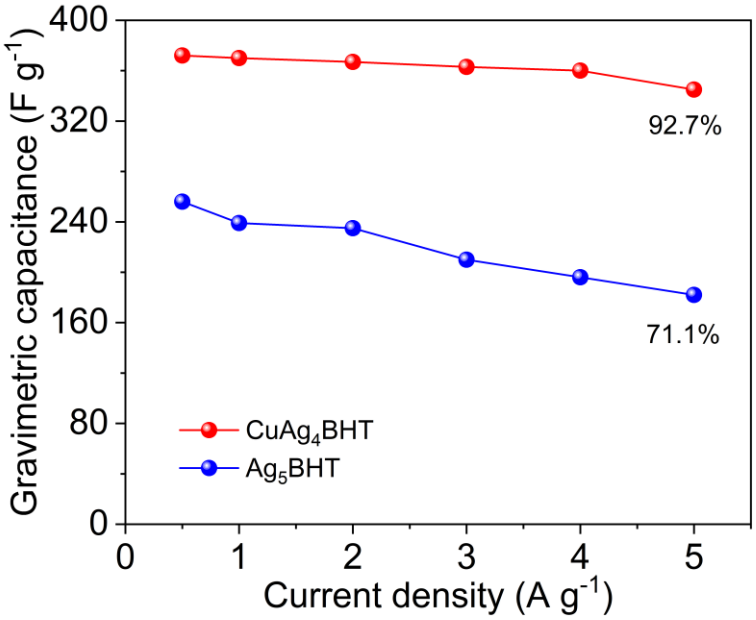

Figure S17. The comparison of gravimetric and areal capacitances of Ag_5BHT and $CuAg_4BHT$ at the different current densities.

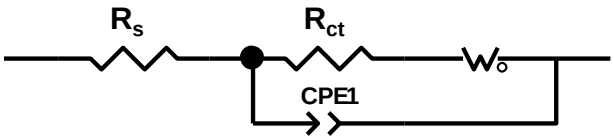

Figure S18. Equivalent circuit of the CPs electrodes. R_s is the equivalent series resistance, R_{ct} is charge transfer resistance, W_0 represents Warburg diffusion process, CPEl is electrical double-layer capacitance.

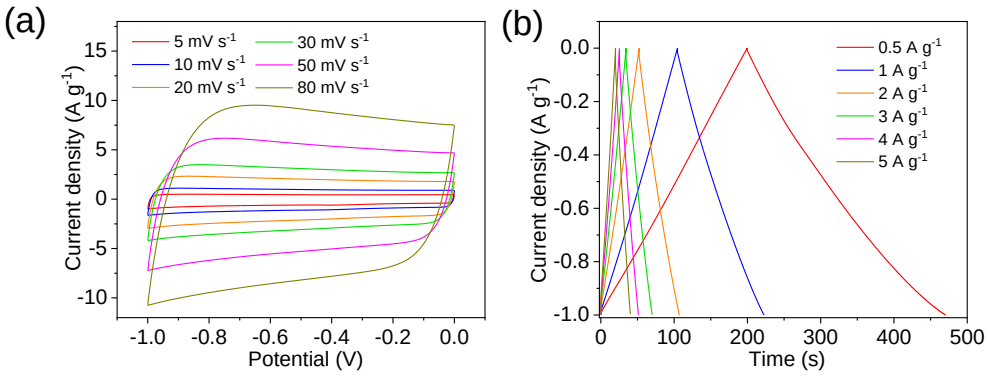

Figure S19. The CV curves and GCD curves of AC electrode.

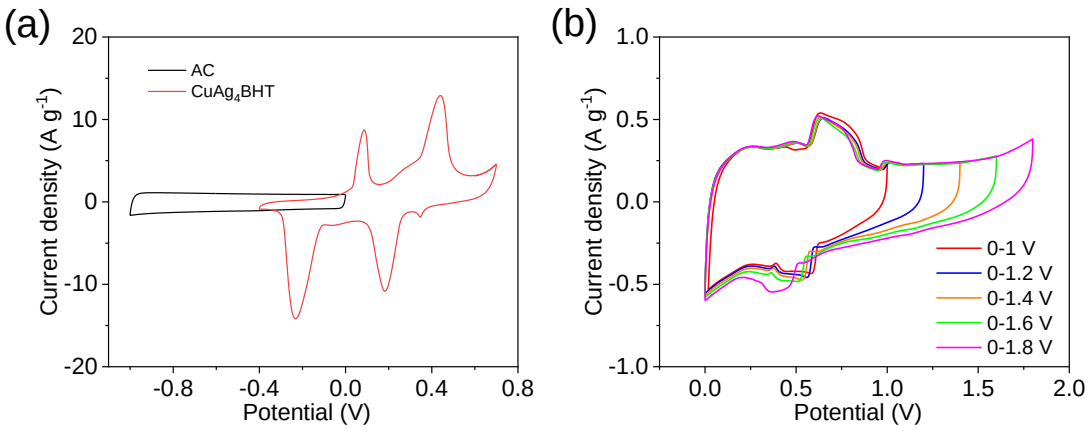

Figure S20. (a) The potential windows of the AC and $CuAg_4BHT$ electrodes at the scan rate 10 mV s^{-1}. (b) The CV curves of assembled devices at different potential windows.

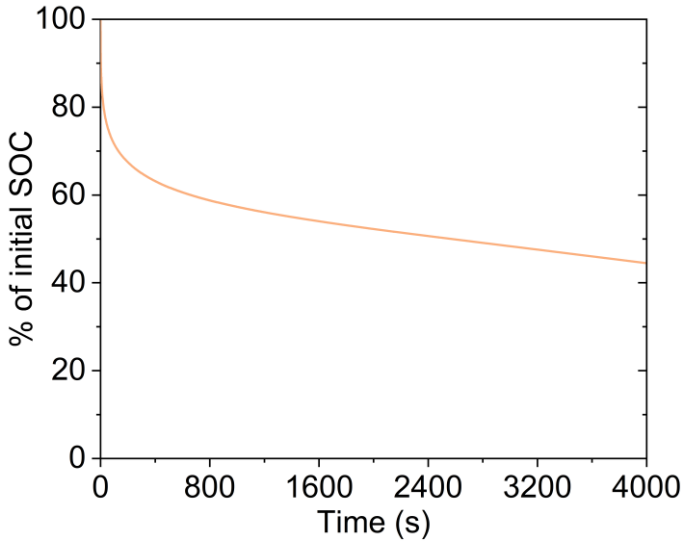

Figure S21. Charge retention over time, presented as percentage of initial state of charge.

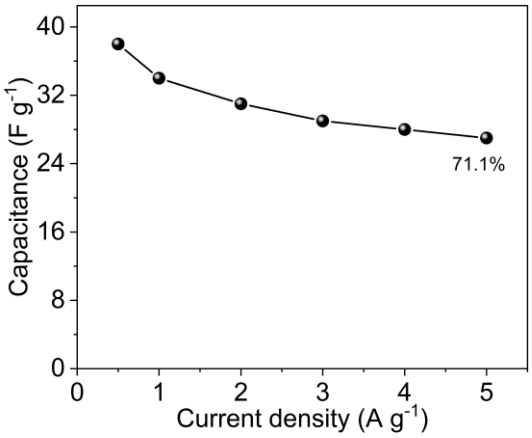

Figure S22. The gravimetric capacitance of $CuAg_4BHT$//AC SC device at different current density.

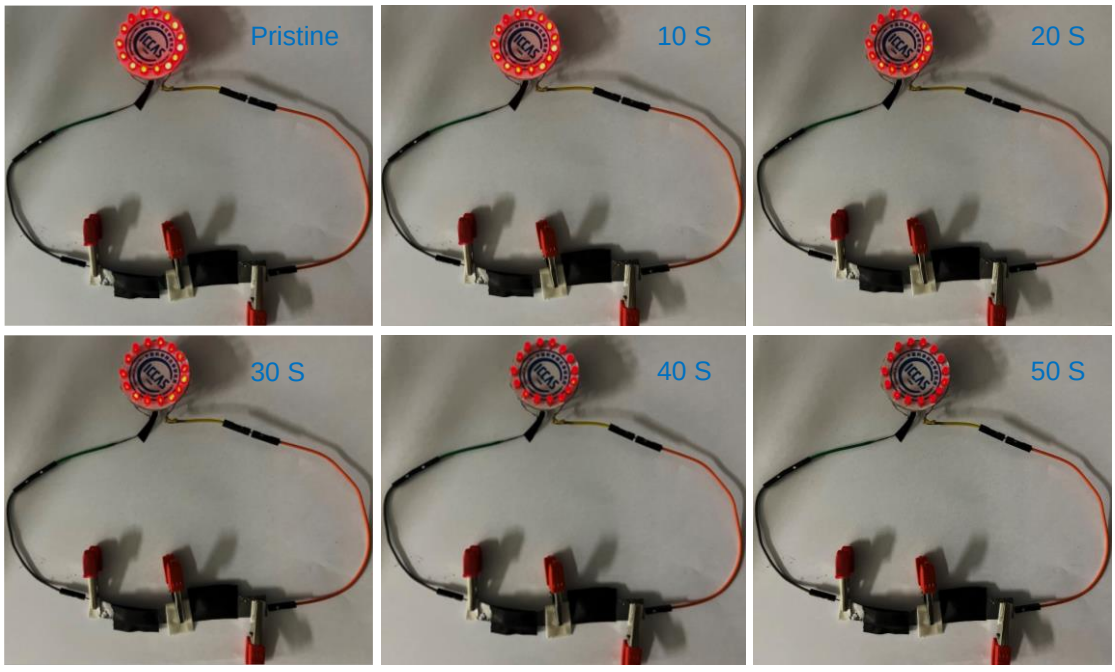

Figure S23. Pictures of 15 red LEDs (in parallel) lighted up by two prepared devices in series.

Table S1. Performance comparison of different electrode materials in liquid electrolytes (three-electrode setup, at 0.5 A g^{-1}).

Materials	Gravimetric capacitance /F g^{-1}	Potential window /V	Electrolyte	Ref.
$CuAg_4BHT$	372	-0.4~0.7	1 M KCl	This work
Ag_5BHT	256			
Cu_3BHT	312			
Cu_4BHT	190	-1.2~0	1 M KCl	1
$Cu_{5.5}BHT$	95			
Cu-DBC	368	-0.5~0.2	1 M NaCl	2
$Ni_3(HIB)_2$	410	-0.75~-0.25	1 M KOH	3
$Ni_3(HITP)_2$	112	0~0.7	3 M KCl	4
$Cu_3(HHTP)_2$	202	0~0.5	3 M KCl	5
$Ni_3(HITP)_2$	83	-0.6~0.5	1M $TEABF_4$/ACN	6
CuO nanoflakes	190	0~0.6	1 M KOH	7
Graphene	198	0~1.0	1 M H_2SO_4	8
Nitrogen-doped activated carbon	255	0~-0.1	2 M KOH	9
Activated graphene	202 (1 A g^{-1})	/	1 M $TEABF_4$/AN	10
Porous carbon	280	0~1.0	6 M KOH	11
Nano-porous MXene	351	-0.5~0.3	3 M H_2SO_4	12
Hierarchical porous carbon	240	-0.2~0.9	1 M H_2SO_4	13

Table S2. Performance comparison between $CuAg_4BHT$//AC device and other devices assembled by some reported MOFs.

SC devices	Energy density (Wh kg^{-1})	Power density (W kg^{-1})	Energy density (Wh kg^{-1})	Power Density (W kg^{-1})	Ref.
$CuAg_4BHT$//AC	17.1	446.1	12.2	4374.0	This work
Cu-DBC//Cu-DBC	13.8	100	7.6	5000	2
Ni-HAB//Ni-HAB	14.8	21	11.6	419	3
MnO_2//AC	17.5	135	12.8	2197	14
Co-PCN//AC	16	749	9	9000	15
Co_9S_8/NS-C//AC	14.85	681.8	6.63	6818.2	16
$Co(OH)_2$-nanowires//AC	13.6	153	13.1	1880	17
Ni/Co-MOF//AC	20.9	800	15.8	4000	18

References

1. Sun Y. et al. The Increasing Number of Electron Reservoirs in Nonporous, High-Conducting Coordination Polymers Cu_x BHT (x = 3, 4, and 5, BHT = Benzenehexathiol) for Improved Faradaic Capacitance. *Small* **18**, e2203702 (2022).
2. Liu J. et al. Conjugated Copper-Catecholate Framework Electrodes for Efficient Energy Storage. *Angew. Chem. Int. Ed.* **59**, 1081-1086 (2020).
3. Feng D. et al. Robust and conductive two-dimensional metal−organic frameworks with exceptionally high volumetric and areal capacitance. *Nat. Energy* **3**, 30-36 (2018).
4. Zhou S. et al. Cellulose Nanofiber@Conductive Metal-Organic Frameworks for High-Performance Flexible Supercapacitors. *ACS Nano* **13**, 9578-9586 (2019).
5. Li W.-H. et al. Conductive Metal-Organic Framework Nanowire Array Electrodes for High-Performance Solid-State Supercapacitors. *Adv. Funct. Mater.* **27**, 1702067 (2017).
6. Sheberla D. et al. Conductive MOF electrodes for stable supercapacitors with high areal capacitance. *Nat. Mater.* **16**, 220-224 (2017).
7. Endut Z., Hamdi M. & Basirun W. J. Pseudocapacitive performance of vertical copper oxide nanoflakes. *Thin Solid Films* **528**, 213-216 (2013).
8. Yang X., Cheng C., Wang Y., Qiu L. & Li D. Liquid-mediated dense integration of graphene materials for compact capacitive energy storage. *Science* **341**, 534-537 (2013).
9. Ma G. et al. Nitrogen-doped porous carbon derived from biomass waste for high-performance supercapacitor. *Bioresour. Technol.* **197**, 137-142 (2015).
10. Zhang L. et al. Porous 3D graphene-based bulk materials with exceptional high surface area and excellent conductivity for supercapacitors. *Sci. Rep.* **3**, 1408 (2013).
11. Shang T. et al. A bio-derived sheet-like porous carbon with thin-layer pore walls for ultrahigh-power supercapacitors. *Nano Energy* **70**, 104531 (2020).
12. Fan Z. et al. A nanoporous MXene film enables flexible supercapacitors with high energy storage. *Nanoscale* **10**, 9642-9652 (2018).
13. Li Q. et al. Fabrication of Ordered Macro-Microporous Single-Crystalline MOF and Its Derivative Carbon Material for Supercapacitor. *Adv. Energy Mater.* **10**, 1903750 (2020).
14. Li H. H., Zhang X. D., Ding R., Qi L. & Wang H. Y. Facile synthesis of mesoporous MnO_2 microspheres for high performance AC//MnO_2 aqueous hybrid supercapacitors. *Electrochim. Acta* **108**, 497-505 (2013).
15. Wang K. et al. Porous Cobalt Metal-Organic Frameworks as Active Elements in Battery-Supercapacitor Hybrid Devices. *Inorg. Chem.* **59**, 6808-6814 (2020).
16. Zhang S. et al. Highly stable supercapacitors with MOF-derived Co_9S_8/carbon electrodes for high rate electrochemical energy storage. *J. Mater. Chem. A* **5**, 12453-12461 (2017).
17. Tang Y. F. et al. Morphology controlled synthesis of monodisperse cobalt hydroxide for supercapacitor with high performance and long cycle life. *J. Power Sources* **256**, 160-169 (2014).
18. Gao S. et al. Dandelion-like nickel/cobalt metal-organic framework based electrode materials for high performance supercapacitors. *J. Colloid Interface Sci.* **531**, 83-90 (2018).